

Automatic focus method using interference fringes magnitudes in retinal optical coherence tomography

Ming Liu¹,^{a,†} Xinjian Chen,^{a,†,b} and Bo Wang^{a,*}

^aSoochow University, School of Electronic and Information Engineering, Suzhou, China

^bSoochow University, State Key Laboratory of Radiation Medicine and Protection, Suzhou, China

Abstract. In retinal optical coherence tomography (OCT), it is significant to focus the scan beam on the retina layers of the human eye fast to acquire high-quality OCT images. The refractive errors of the human eye are usually compensated by shifting the optical lens in the sample arm manually or electrically. Otherwise, refractive errors of the human eye will cause axial focal shift of the scanning beam and blur the OCT images. We propose a fast automatic focus method using the interference fringes magnitudes of the whole retinal layers to determine the best refractive correction position of motor-driven optical compensation lens without the aid of optical fundus imaging or OCT B-scan imaging. Also, the optical path difference between the sample arm and reference arm is adjusted in the spectral-domain OCT (SD-OCT) to reduce the effects of sensitivity roll-off. The experiments in the lab-built SD-OCT show that the average running time of the method is 15.2 s and the mean absolute deviation of each imaging is within 1 mm. The method is independent of extra optical setup and requires less computational consumption, which is suitable for low-cost and automatic retinal OCT devices. © 2021 Society of Photo-Optical Instrumentation Engineers (SPIE) [DOI: [10.1117/1.OE.60.XX.XXXXXX](https://doi.org/10.1117/1.OE.60.XX.XXXXXX)]

Keywords: ophthalmology optical coherence tomography; refractive correction; interference fringes magnitudes.

Paper 20210422 received Apr. 19, 2021; accepted for publication Aug. 24, 2021.

1 Introduction

Retinal optical coherence tomography (OCT) has been used as the ground truth to diagnose and monitor various eye diseases, such as glaucoma, macular hole, age-related macular degeneration, and diabetic macular edema.¹⁻³ In the clinical applications, it pursues better image quality and operation convenience of the retinal OCT devices for correct and rapid assistant diagnosis.

To acquire high-quality retina OCT images, it is critical to correct refractive errors of the human eye.⁴ Nowadays, many people suffer from myopia or hyperopia at various ocular diopter values, which prevents incident parallel rays from focusing on the same position when compared to an emmetropic eye.⁵ In the OCT sample arm, optical compensation lenses, such as movable lens(es) or variable-focus liquid lens(es), are usually adopted to tune the divergence/convergence of the beam incident on the pupil, which leads the scanning beam to focus on the retina layers of the ametropic eye.

However, additional imaging modalities are often needed in the sample arm to assist the adjustment of optical compensation lens(es) for best refractive correction, especially in the manual operation mode. The imaging techniques such as fundus imaging, confocal scanning laser ophthalmoscopy,⁶ and line scanning ophthalmoscopy can be designed coaxially with refractive correction lens(es) for operator indication. Thus, the operator can adjust the focus of retina layers through the preview fundus images and then the optical path difference (OPD) between the reference arm and scanning beam to get the OCT B-scan images. In these methods, the adjustment of the sample arm and reference arm is step by step, which is easy to follow. But it will increase the cost of optical design and fabrication. The focus method using

*Address all correspondence to Bo Wang, wangbo@suda.edu.cn

[†]These authors contributed equally.

only OCT B-scans is also proposed,⁷ which is without the additional optical fundus imaging. The brightness of the selected layer within the selected *en face* is used as the metric of the optimization process. The optimization is fast and suitable for automatic focus control. But the layer segmentation algorithm is implemented in the GPU processing platform for acceleration, which is heavy computation.

There are certain common strategies for increasing the signal-to-noise (SNR) of retinal OCT images after refractive correction. Different uncorrelated speckle patterns are recorded by angular compounding,⁸ frequency compounding,⁹ etc., to average speckle noises. Wavefront sensing and wavefront correction devices are utilized in adaptive optical OCT to set the focus on the selected layer to reduce imaging speckle and limited depth of focus.^{4,10} Nevertheless, these hardware-based approaches require complex modifications and further acquisition of data that are difficult to integrate directly in clinical ophthalmology OCT scanners. In software-based approaches, algorithms such as spatial filtering^{11,12} and sparse transform^{13,14} are employed to improve the SNR of OCT images. Moreover, statistical model-based methods^{15,16} and deep learning methods^{17,18} are popular nowadays due to the flexibility of modeling and a large amount of data. But regarded as post-processing strategies, these software-based methods are hard to improve a defocused OCT B-scans.

In this paper, we propose an automatic focus method using interference fringes magnitudes as an optimization metric, which saves the additional imaging hardware and GPU computation resource. Unlike the manual focus operation, which adjusts refraction errors in the sample arm and OPD in the reference arm step by step, the proposed focus method adjusts OPD in the reference arm to find the interference fringes of retina layers first. Then it locks the OPD to a fixed position where the value of OPD is about 1 mm to ensure the high SNR in spectral-domain OCT (SD-OCT) and the choroid layer is close to the zero OPD position. Finally, the hill-climbing method is utilized to find the best refractive correction position in the sample arm, which shows the strongest interference fringe magnitude. The calculation of the fringe magnitude does not need the k -linearization and FFT steps, which can save computational time and resources.

2 Experimental Setup of the Retinal OCT

We build an SD-OCT setup instead of swept-source OCT for cost consideration shown in Fig. 1(a). The output of the Superlum SLD source centered at 840 nm with a 45-nm bandwidth is split into sample arm fiber and reference arm fiber by an 80:20 coupler. The reflective mirror in the reference arm is located in the motor-driven stage to adjust OPD. In the sample arm, the classical relay lens and objective lens configuration is adopted for refractive correction by varying the distance between the two lenses. A fixation target is also designed to help fixing the visual axis of the eye. The relay lens in the sample arm is also located at a motor-driven stage instead of the objective lens. The high-speed spectrometer is built with a volume grating (Wasatch optics, 1800 lines/mm) and a USB linear camera (e2v, 80 kHz).

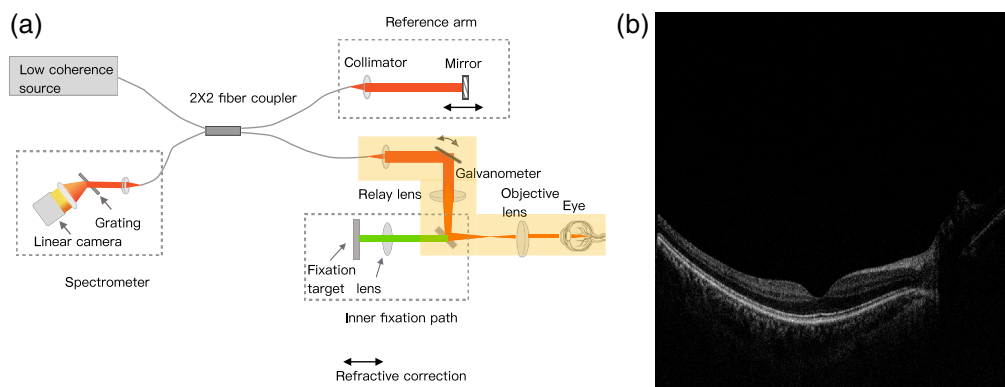


Fig. 1 Retinal OCT setup using SLD and spectrometer: (a) optical setup and (b) the retinal B-scan through fovea.

The low-coherence light interference fringes are recorded by the spectrometer when the backscattered light from the sample arm and reference arm are coherent. The recorded signals need Fourier transform processing to obtain OCT images.¹⁹ Generally, the following steps are required.¹⁹

1. Wavelength calibration: map the spectrometer camera pixel index to wavelength.
2. Background subtraction: remove the fixed-pattern noise and direct current terms to a clear interference fringes pattern.
3. k -linearization: resample the fringes in k space evenly.
4. IFFT: implement inverse Fourier transformation to calculate the depth profile from the pre-processed fringe pattern. Each fringe pattern produces an A-scan profile.
5. Truncate and logarithm of B-scan: the symmetric part of IFFT results is truncated to avoid displaying duplicate images and reduce image size. The logarithm of the B-scan performs dynamic range compression for better visualization.

In Fig. 2, the OCT signal/image of a metal plate out of imaging depth and within the imaging depth (OPD = 1.0 mm) from raw data to B-scan in the reconstruction steps are shown. The significant magnitude of interference fringes can be observed in the raw data and after background subtraction and k -linearization. In the A-scan and B-scan, the reflection peaks of the metal plate surface are also obvious. In Fig. 2(f), the interference fringes after background subtraction behave strong oscillation with a large magnitude. In Fig. 2(g), strong interference peak resulted by the surface of metallic plate is shown in A-scan whose magnitude is significantly higher than the noise. These results show the capability of interference fringes as a focus optimization metric.

3 Automatic Focus Optimization Algorithm

3.1 Find the Interference Signal and Determine the Imaging Position

In the automatic focus algorithm, the interference fringe of the retina should be found first for subsequent optimization calculations. The distance between the relay lens and objective lens in the sample arm is initialized with a guess value, where the ocular diopter is equal to 0. Then a large search range of about 45 mm in the reference arm is set to search the interference signals according to the optical design. After that, the image height and direction should be determined based on the algorithm. The parameters obtained through the algorithm are sent to the STM32 chip to control the stepper motor through microstepping. Microstepping is a way of moving the stator flux of a stepper more smoothly than in full- or half-step drive modes.²⁰ This results in less vibration and noiseless stepping. It also makes smaller step angles and better positioning possible.

Due to the sensitivity roll-off caused by the spatial sampling of spectrometer camera pixel in SD-OCT, two modes (the retina layers is close to OPD = 0 or the choroid layers is close to OPD = 0 in the OCT image) should be selected in real applications. Because of the ellipsoid-like eye structure, if the retina is close to the position of OPD = 0 during imaging, the tissue structure can be observed to be convex; if the choroid is close to the position of OPD = 0, the tissue structure can be observed to be concave. To prevent the retinal structure from turning over at OPD = 0 in OCT images, considering that the thickness of the retinal layer is about 0.3 mm, the retinal structure can be fixed in the place where OPD > 0.5 mm. The image of our SD-OCT system designed in this paper is defined as shown in Fig. 1(b). The bottom of the image is the position where OPD is zero, and the choroid is at the bottom. The retinal structure is fixed at a height of 100 pixels above the bottom of the image (corresponding to an OPD of about 0.5 mm).

To determine the imaging position, the approximate depth and direction of the retinal structure should be calculated. The depth of retina d is defined as

$$d = \arg \min_i \sum_{j=1}^N I(i, j), \quad (1)$$

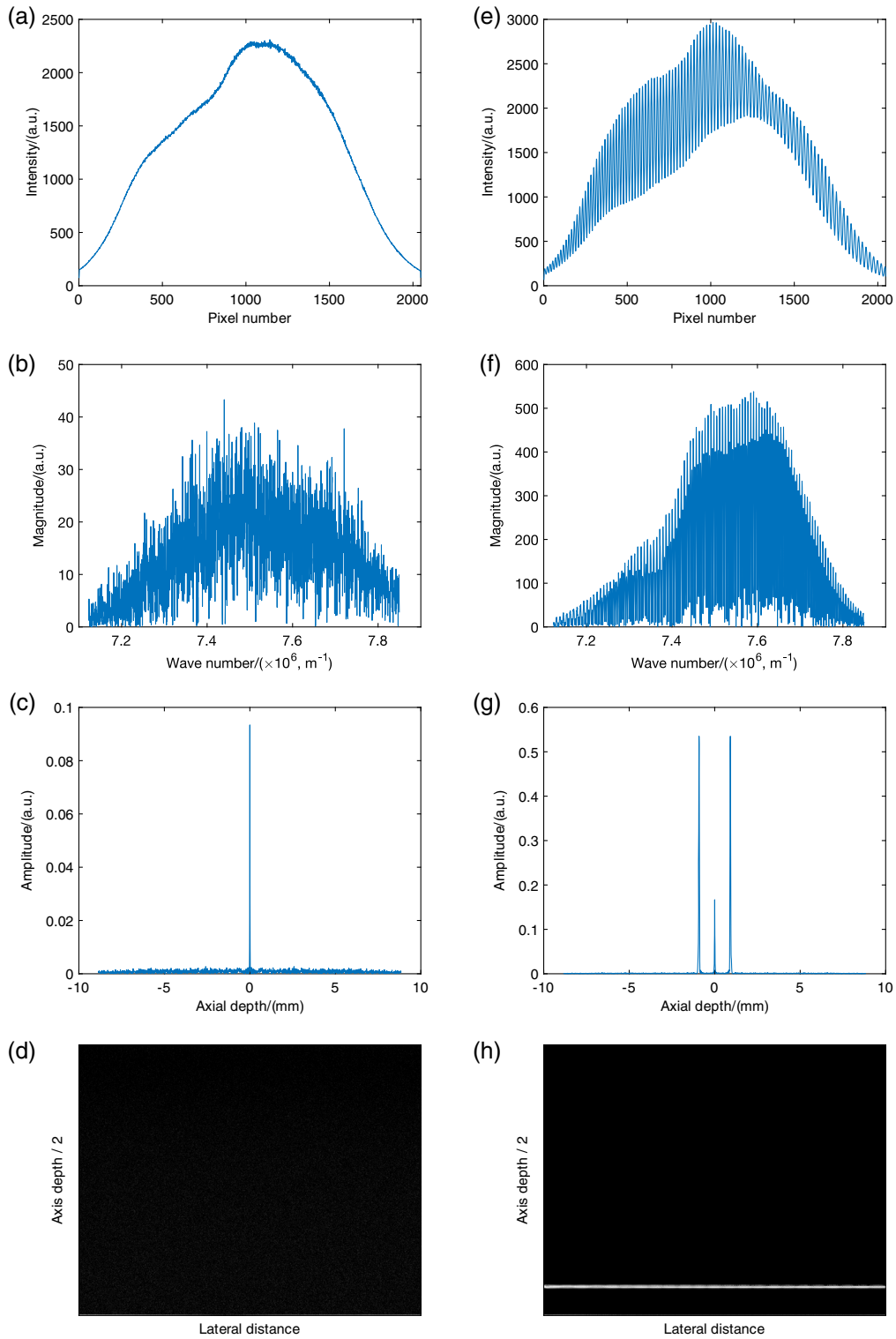


Fig. 2 The signal processing process in SD-OCT (take a metal plate as the sample). (a) The origin signal without interference is a smooth curve that approximates the spectral shape of the light source. (b) The faint random thermal noise of only 13.12 average and 43.31 maximum magnitude after background subtraction. (c) The A-scan profile with only one peak of DC noise after k -linearization and IFFT. (d) The final B-scan without any target information. (e) The origin signal with interference is an oscillating curve superimposed on the reference light intensity similar to a sinusoidal modulation. (f) A strongly oscillating signal spectrum of 153.41 average magnitude, which is 12 times of (b). (g) The A-scan profile with two interference peaks at a specific position in addition to the DC peak. (h) The metal plate can be observed at the corresponding depth in the final B-scan.

where I is the reconstructed image with the size of $M \times N$, i, j are coordinates in the longitudinal and lateral direction in the image, and $\arg \min$ operator represents the value of i when the function value is minimized.

When calculating the concave and convex direction of the retina in the reconstructed image, the image should be equally divided into three regions I_a, I_b , and I_c and the average rows R_a, R_b, R_c in the three regions are calculated, respectively. The formula is as follows (take R_a as an example):

$$R_a = (\arg \min_i I_a(i, j_1)) + \arg \min_i I_a(i, j_2) + \arg \min_i I_a(i, j_3)) / 3, \tag{2}$$

where j_1, j_2 , and j_3 are the three A-scans of equally dividing I_a . If the sum of R_a and R_c is smaller than twice of R_b , the direction of the retina is determined to be concave; otherwise, the direction of the retina is determined to be convex.

The algorithm initializes the motor positions of the sample arm and reference arm to a preset search range, which is dependent on the optical design. In the range, the equal optical path position can be quickly determined. Then OPD is tuned to set the retinal layers at the preset image depth and direction.

If constant eye motions are caused by breath and heartbeat in the focusing, the algorithm continues to run to reach the set conditions for the next step. Since the target is designed in the system to help fixation, these eye movements are relatively small. If the eye movements are larger than about ± 1 mm, the algorithm may fail because most of the scanning light is blocked by the pupil.

3.2 Optimize to Find the Best Refractive Correction Position

The sample arm is designed to compensate $-20D$ to $25D$ optically based on the Gullstrand eye models. The process of refractive correction is to make the scanning beam accurately focus on the retina.

To reduce the probability of eye movement or blinks in scanning time, fast refractive correction operations are required during the OCT scanning. The autofocus method needs to calculate the evaluation function to quickly find the in-focus position. Therefore, the evaluation function and the focus search strategy with excellent performance are very important to be chosen.

The focus evaluation function should have a distinct peak at the focus and monotonically and symmetrically decrease on either side of the focal plane.²¹ The value of the evaluation function should become minimum in the autofocus algorithm. In the following, we propose five evaluation functions corresponding to the OCT signal processing process (Table 1).

Table 1 Evaluation functions of refractive correction.

Number	Formula	Description
1	$F_{\text{Spectrum}} = \sum_j \sum_i S_{r-s}(i, j)$	S_{r-s} is the interference signal in ROI, and i, j are coordinates in the longitudinal and lateral direction in the interference fringe.
2	$F_{\text{AscanLinear}} = \sum_j \sum_i S_{r-l}(i, j) / N_r$	S_{r-l} is the linear signal after FFT in ROI and N_r is the columns of ROI.
3	$F_{\text{AscanLog}} = \sum_j \sum_i I_r(i, j) / N_r$	I_r is the reconstructed image of ROI after logarithmic filtering and N_r is the columns of ROI.
4	$F_{\text{Reblur}} = \left(\frac{D_x(I_b)}{D_x(I)} + \frac{D_y(I_b)}{D_y(I)} \right) / 2$	D_x and D_y are the absolute value of the gray intensity deviation of adjacent pixels in the horizontal and vertical directions of the image, respectively.
5	$F_{\text{Brenner}} = \sum_j \sum_i I(i+2, j) - I(i, j) ^2$	I is the reconstructed image, and i, j are coordinates in the longitudinal and lateral direction of I .

1. The signal magnitude of interference fringe after background subtraction in the uniform wavenumber space.
2. A-scan signal intensity value after Fourier transform.
3. A-scan intensity value in log domain based on the reconstructed image.
4. The reblurring method²² to calculate the clarity of B-scan.
5. Brenner gradient function²³ to calculate the clarity of B-scan.

The macula and optic disc in the retina are the concentrated areas of the optic nerve and oxygen supply vessels, respectively, and they are also important areas with a high incidence of various fundus diseases. In OCT imaging, the macula/optic disc is often located in the middle area of the image for observation. Therefore, when calculating the signal magnitude, only the spectral signal in the middle area is selected as the region of interest (ROI) to calculate the evaluation function.

The comparison of normalized values in autofocusing figure-of-merits is shown in Fig. 3(a). Due to the laser safety, the human eyes cannot withstand the long-term exposure of the OCT scanning beam. Also, it is difficult to ensure the same position during multiple measurements due to eye movement. Therefore, a phantom eye (OCULAR OEMI-7) is utilized for the comparison test of the five evaluation functions shown in Fig. 3(b). After the position of the equal optical path is determined, move the diopter motor and the optical path motor with a step of 0.5 mm at the same time, and calculate the focus evaluation function in every step. As shown in Fig. 3(a), in the curve of F_{Spectrum} , there is a sharp, distinct peak at the focus, and smooth rapid dropping away from focus. It shows F_{Spectrum} is the most sensitive function among the five functions. Also, the magnitude of the interference fringe signal can be calculated without image reconstruction, which can save the computational time. As a result, we select F_{Spectrum} as the evaluation function for autofocusing.

The focus search strategy is another key technology of autofocusing. In the past, typical focus search methods are presented such as curve fitting method, global search method, golden section method, and hill-climbing method.²⁴⁻²⁷ Most of the curve fitting methods²⁸ only find similar function expressions based on the shape of the evaluation function. It takes excessive time using the global search method because the entire focus search range is traversed. But it would be a challenge for human eyes to keep fixation in a long duration. The golden section method keeps narrowing the search range according to the golden ratio (0.618). However, the focus evaluation function is more random, and it is easy to judge the search direction wrongly in the first iteration.

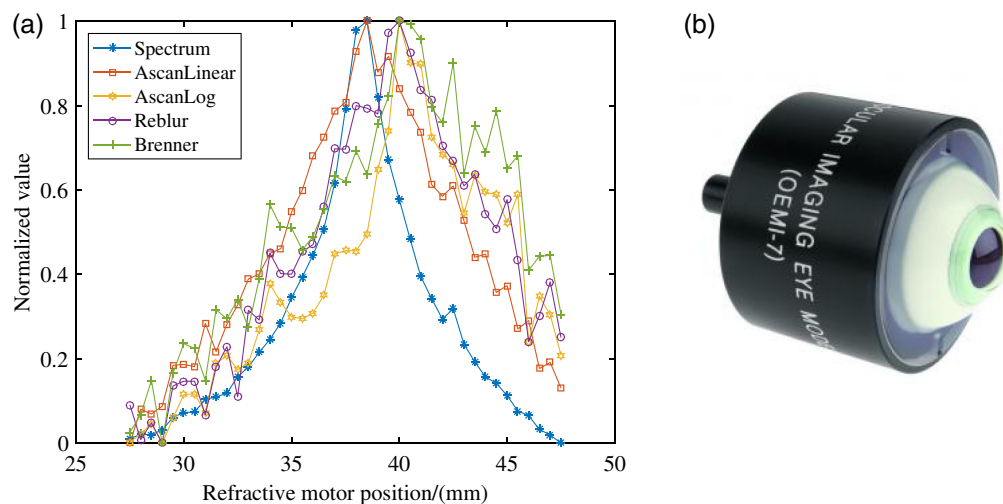


Fig. 3 Comparison of normalized values in autofocusing figure-of-merits by imaging the phantom eye. (a) Normalized curves of different indicators and (b) the phantom eye. The F_{Spectrum} is considered as the most sensitive function with a sharp, distinct peak at the focus, and a rapid drop away from focus.

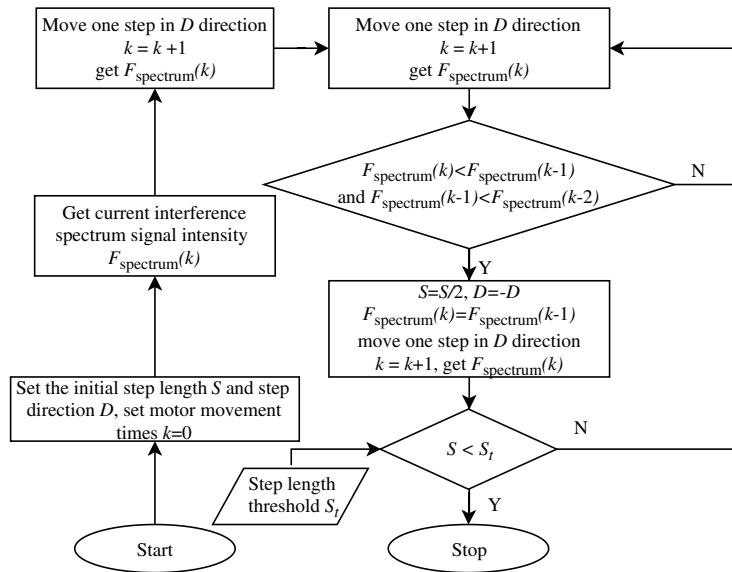


Fig. 4 Flowchart of refractive correction based on hill-climbing method.

As the evaluation function curve based on the interference signal magnitude is parabolic and has good unimodality, we choose the hill-climbing method to search the in-focus position.

The hill-climbing method judges the search direction by comparing the evaluation functions of different positions. If the evaluation value drops twice in one iteration, it is determined that it is in a downhill state or has crossed the peak value. In addition, in view of the problem of multiple small peaks, we can increase the initial step length to avoid the local maximum and quickly limit the search range to the vicinity of the main peak since the small peaks are often far from the main peak. The flowchart of refractive correction based on the hill-climbing method is shown in Fig. 4.

4 Experiments and Results

To evaluate the performance of the proposed method, the SD-OCT system is built and the optical setup is shown in Fig. 1(a). The codes were implemented in C++/OpenCV and tested on a PC with Intel i7-7700 CPU at 3.60 GHz and 8 GB of RAM.

4.1 Evaluation of the Phantom Eye with Different Diopter Values

Due to too many factors affecting human eye imaging and the inconvenience of the manual locating at each time, the phantom eye with different diopter values is first tested to assess the speed and accuracy of the algorithm. Spherical lenses with negative and positive diopter (accessories of NIDEK Refractor RT-6100) are placed in front of the phantom eye to simulate different diopter values. The average running time of the method with all procedures is calculated by recording the running time in each measurement. And the quantitative metric of mean absolute deviation (MAD) is utilized to measure the accuracy of the algorithm, which is formulated as

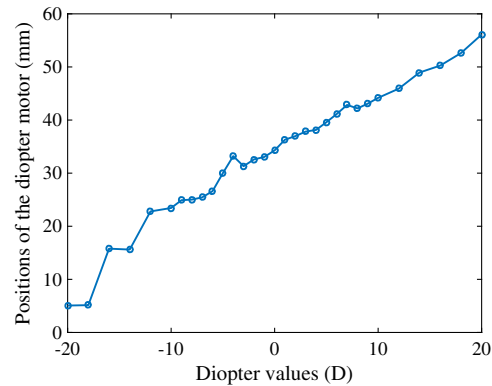
$$MAD = \frac{\sum_{i=1}^n |x_i - \bar{x}|}{n}, \quad (3)$$

where n is the number of measurements, x_i is the position of the diopter motor in each measurement, and \bar{x} is the mean value of these positions.

The spherical lenses of 0D, +20D, and -20D are placed in front of the phantom eye to cover the general and extreme situations. The measurements are repeated 20 times for each diopter value. The results of the running time and the accuracy metric of MAD are shown in Table 2. The mean running time of the algorithm is 15.2 s and the mean MAD value is 0.94 mm, which represents the high accuracy of our method. In addition, the entire range of the diopter values

Table 2 Evaluational results of the quantitative metrics.

Diopter (D)	Time (s)	MAD (mm)
-20	18.68	1.28
0	14.31	0.34
+20	12.80	1.21
Mean	15.20	0.94

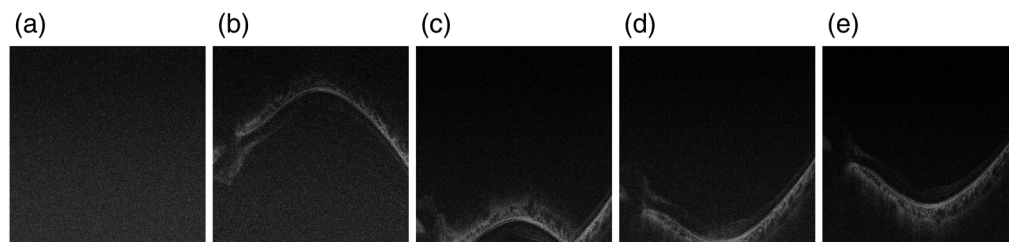
**Fig. 5** The positions of the diopter motor as the function of various diopter values. The position of the motor changes continuously with the diopter value.

is tested by imaging 3 times at each diopter. The resolution of -20D to -10D and 10D to 20D is set to 2D and the resolution between -10D and 10D is set to 1D because fewer people are myopia and hyperopia of high diopter values. The curve between the positions of the diopter motor in sample arm and different diopter values is shown in Fig. 5. The position of the motor changes continuously with the diopter value.

4.2 Evaluation of the In-Vivo Eyes

The collection and measurement of human retinal image data in this research are approved by the Ethics Committee of Soochow University. The algorithm is also verified by volunteers under the premise of ensuring the safety of laser power. All eligible subjects received an explanation of the study and signed an informed consent form in accordance with the principles embodied in the Declaration of Helsinki.

Before autofocusing, the position of the equal optical path should be found and the retinal structure will be at the appropriate imaging position. The intermediate results of determining the retinal imaging position are shown in Fig. 6. In Fig. 6(a), the OPD exceeds the coherence length

**Fig. 6** Determining retinal imaging position. (a) Reconstructed image without interference; (b)–(d) the change process of imaging position when stepping the optical path motor; and (e) reconstructed image of retina at the proper imaging position. The retinal imaging position is determined well using the proposed algorithm.

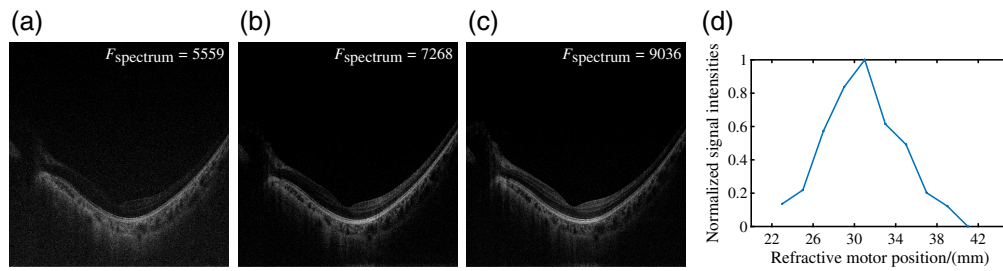


Fig. 7 Autofocusing of the proposed algorithm. (a) Reconstructed image when the imaging position is just determined; (b) reconstructed image during optimization process; (c) reconstructed image of retina after refractive correction; and (d) the curve of normalized signal intensities by imaging the *in-vivo* eye. The retinal structure in the image with the highest fringe magnitude after autofocusing is more detailed and clear.

of the light source, and the retinal structure is not found. Figures 6(b), 6(c), and 6(d) show the changes in the retinal imaging position when moving the motor in reference arm. The image first shows that the retina is close to the position of the equal optical path (the retinal structure is convex), then it is folded at the position of the equal optical path, and then the choroid is close to the equal optical path position (the retinal structure is concave). Finally, the retinal structure at the proper imaging position is shown in Fig. 6(e).

After obtaining the retinal structure at an appropriate imaging position, the intermediate reconstructed B-scans of the autofocusing process are shown in Fig. 7, where the values of the focus evaluation function are calculated and displayed at the top right corner of each image. When the imaging position is just determined, the signal intensity of the interference fringe is 5559 shown in Fig. 7(a). The reconstructed B-scan with incomplete refractive correction during the hill-climbing method, whose signal intensity of the interference fringe is 7268, as shown in Fig. 7(b). The reconstructed B-scan after the automatic refractive correction is completed as shown in Fig. 7(c). The signal intensity of the interference fringe is 9036, which reaches the maximum value. It can be seen from the B-scan that the retinal structure is more clear after autofocusing with sharper edges of the retinal layers and more details such as vessels or smaller lesions in the inner retinal area. The curve of normalized signal intensities of the interference fringe versus the reflective motor position is illustrated in Fig. 7(d). The computational time to reconstruct an image is about 248 ms, whereas the time to calculate the signal intensity of the interference fringe is only about 10 ms, which can almost be ignored.

The algorithm proposed in this paper needs to consider both real-time processing and stability. To reduce total data acquisition time, the step length of the motor can be increased, but this will reduce the stability of the algorithm. Especially when looking for the position of the equal optical path, the retina can only be captured 1 to 2 times during the motor stepping process with a large step length. If the subject blinks at this moment, the retinal structure may not be captured, thus missing the position of the equal optical path and making the motor continue to step, which may cause the algorithm to fail. Also, during the refractive correction, if the unintentional eye/head motions are too large and the retina is out of the imaging range, the refractive correction algorithm will fail. If the algorithm fails, manual operations are needed to fix the situation.

5 Conclusion

In this paper, we propose a focus method using the interference fringes magnitudes of the whole retinal layers to correct refractive errors and adjust the OPD between the sample arm and the reference arm. An SD-OCT setup with motor-driven sample arm and reference arm is built to demonstrate the effectiveness of the method. The method can avoid the process of image reconstruction and subjective judgments of image quality to complete the autofocusing quickly and accurately. Moreover, it does not require additional optical imaging design, which is a low-cost but practical system to simplify manual operation.

Acknowledgments

We are very grateful to Bigvision Medical Technology Co. Ltd. for the technologies they provided about the stepper-motor control and reference arm design. Disclosures: The authors declare that there are no conflicts of interest related to this article. Funding: This work was supported in part by the National Key R&D Program of China under Grant No. 2018YF-A0701700 and in part by the National Natural Science Foundation of China (NSFC) under Grant No. 61622114.

References

1. G. J. Jaffe and J. Caprioli, "Optical coherence tomography to detect and manage retinal disease and glaucoma," *Am. J. Ophthalmol.* **137**(1), 156–169 (2004).
2. J. G. Fujimoto et al., "Optical coherence tomography (OCT) in ophthalmology: introduction," *Opt. Express* **17**(5), 3978–3979 (2009).
3. M. Azimipour et al., "Coextensive synchronized SLO-OCT with adaptive optics for human retinal imaging," *Opt. Lett.* **44**, 4219 (2019).
4. M. Pircher and R. J. Zawadzki, "Review of adaptive optics OCT (AO-OCT): principles and applications for retinal imaging," *Biomed. Opt. Express* **8**, 2536–2562 (2017).
5. M. Kaschke, K. H. Donnerhacke, and M. S. Rill, *Optical Visualization, Imaging, and Structural Analysis*, Chapter 6, pp. 147–276, John Wiley and Sons, Ltd. (2014).
6. J. Yi et al., "Human retinal imaging using visible-light optical coherence tomography guided by scanning laser ophthalmoscopy," *Biomed. Opt. Express* **6**, 3701–3713 (2015).
7. M. Cua et al., "Retinal optical coherence tomography at 1 μm with dynamic focus control and axial motion tracking," *J. Biomed. Opt.* **21**, 026007 (2016).
8. H. Wang and A. M. Rollins, "Speckle reduction in optical coherence tomography using angular compounding by B-scan Doppler-shift encoding," *J. Biomed. Opt.* **14**(3), 030512 (2009).
9. M. Pircher et al., "Speckle reduction in optical coherence tomography by frequency compounding," *J. Biomed. Opt.* **8**(3), 565 (2003).
10. A. Baghaie, Z. Yu, and R. M. D'Souza, "Involuntary eye motion correction in retinal optical coherence tomography: hardware or software solution?" *Med. Image Anal.* **37**, 129–145 (2017).
11. A. Ozcan et al., "Speckle reduction in optical coherence tomography images using digital filtering," *J. Opt. Soc. Am. A* **24**, 1901–1910 (2007).
12. H. M. Salinas and D. C. Fernandez, "Comparison of PDE-based nonlinear diffusion approaches for image enhancement and denoising in optical coherence tomography," *IEEE Trans. Med. Imaging* **26**(6), 761–771 (2007).
13. M. A. Mayer et al., "Wavelet denoising of multiframe optical coherence tomography data," *Biomed. Opt. Express* **3**(3), 572–589 (2012).
14. L. Fang et al., "Segmentation based sparse reconstruction of optical coherence tomography images," *IEEE Trans. Med. Imaging* **36**(2), 407–421 (2017).
15. D. A. Jesus and D. R. Iskander, "Assessment of corneal properties based on statistical modeling of oct speckle," *Biomed. Opt. Express* **8**, 162–176 (2017).
16. M. Li et al., "Statistical model for OCT image denoising," *Biomed. Opt. Express* **8**, 3903–3917 (2017).
17. Y. Ma et al., "Speckle noise reduction in optical coherence tomography images based on edge-sensitive cGAN," *Biomed. Opt. Express* **9**, 5129 (2018).
18. Y. Guo et al., "Structure-aware noise reduction generative adversarial network for optical coherence tomography image," in *Ophthalmic Medical Image Analysis*, H. Fu et al., Eds., pp. 9–17, Springer International Publishing.
19. M. Ali et al., "Low power real time signal processing engine for optical coherence tomography systems using multi-core digital signal processor," *Proc. SPIE* **7889**, 78892J (2011).
20. N. Jirasuwankul and C. Manop, "A lab-scale heliostat positioning control using fuzzy logic based stepper motor drive with micro step and multi-frequency mode," in *IEEE Int. Conf. Fuzzy Syst. (FUZZ-IEEE)*, pp. 1–6 (2017).

21. Y. Sun, S. Duthaler, and B. J. Nelson, "Autofocusing algorithm selection in computer microscopy," in *IEEE/RSJ Int. Conf. Intell. Rob. and Syst.*, pp. 70–76 (2005).
22. B. Wang and J. Tao, "Image clarify detection method and apparatus," Chinese Patent CN106934804A (2017).
23. S. Yazdanfar et al., "Simple and robust image-based autofocusing for digital microscopy," *Opt. Express* **16**, 8670–8677 (2008).
24. Y. Wang et al., "Fast auto-focus scheme based on optical defocus fitting model," *J. Mod. Opt.* **65**(7), 858–868 (2018).
25. M. Liu, X. Chen, and B. Wang, "Axial and horizontal registration guided speckle suppression in single-line HD mode for retinal optical coherence tomography images," *Opt. Commun.* **487**, 126807 (2021).
26. M. Moscaritolo et al., "An image based auto-focusing algorithm for digital fundus photography," *IEEE Trans. Med. Imaging* **28**(11), 1703–1707 (2009).
27. S. S. Chen, D. L. Donoho, and M. A. Saunders, "Atomic decomposition by basis pursuit," *SIAM Rev.* **43**(1), 129–159 (2001).
28. M. Muhammad and T. Choi, "Sampling for shape from focus in optical microscopy," *IEEE Trans. Pattern Anal. Mach. Intell.* **34**(3), 564–573 (2012).

Ming Liu is now a master's student in the Lab of Medical Image Processing, Analysis and Visualization (MIPAV) at Soochow University. He received his BS degree from Soochow University in 2020. His current research interests include optical imaging, medical image processing, and deep learning.

Xinjian Chen received his PhD from the Chinese Academy of Sciences in 2006. He is a distinguished professor at Soochow University, Suzhou, China. He conducted postdoctoral research at the University of Pennsylvania, National Institutes of Health, and the University of Iowa, USA, from 2008 to 2012. He has published over 150 top international journal and conference papers. He is also a senior member of IEEE.

Bo Wang received his BS degree in optical engineering from Capital Normal University and PhD in physics from Harbin Institute of Technology in 2010 and 2015, respectively. He is an assistant professor in the School of Electronic and Information Engineering at Soochow University, China. His current research focuses on the applications of infrared/visible optical coherence tomography in ophthalmology and optometry.